

Article

pubs.acs.org/JACS

Seeded Heteroepitaxial Growth of Crystallizable Collagen Triple 2 Helices: Engineering Multifunctional Two-Dimensional Core-Shell 3 Nanostructures

- 4 Andrea D. Merg, [†] Eric van Genderen, [‡] Alisina Bazrafshan, [†] Hanquan Su, [†] Xiaobing Zuo, [§] 5 Gavin Touponse, [†] Thorsten B. Blum, [‡] Khalid Salaita, [†] Jan Pieter Abrahams, ^{‡,||}
- 6 and Vincent P. Conticello*,†©
- [†]Department of Chemistry, Emory University, Atlanta, Georgia 30322, United States
- 8 [‡]Paul Scherrer Institut, CH-5232 Villigen, Switzerland
- 9 [§]X-ray Science Division, Argonne National Laboratory, Lemont, Illinois 60439, United States
- Center for Cellular Imaging and NanoAnalytics, Biozentrum, University of Basel, CH-4058 Basel, Switzerland
 - Supporting Information

12

13

14

15

16

17

18

19

20

21 2.2

23

24

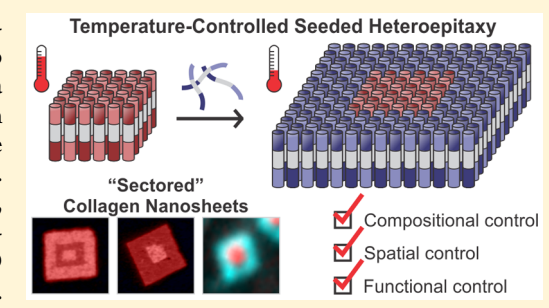
25

26

27

28

ABSTRACT: Engineering free-standing 2D nanomaterials with compositional, spatial, and functional control across size regimes from the nano- to mesoscale represents a significant challenge. Herein, we demonstrate a straightforward strategy for the thermodynamically controlled fabrication of multicomponent sectored nanosheets in which each sector can be chemically and spatially addressed independently and orthogonally. Collagen triple helices, comprising collagen-mimetic peptides (CMPs), are employed as molecularly programmable crystallizable units. Modulating their thermodynamic stability affords the controlled synthesis of 2D core-shell nanostructures via thermally driven heteroepitaxial growth. Structural information, gathered from SAXS and cryo-TEM, reveals that



the distinct peptide domains maintain their intrinsic lattice structure and illuminates various mechanisms employed by CMP triple helices to alleviate the elastic strain associated with the interfacial lattice mismatch. Finally, we demonstrate that different sectors of the sheet surface can be selectively functionalized using bioorthogonal conjugation chemistry. Altogether, we establish a robust platform for constructing multifunctional 2D nanoarchitectures in which one can systematically program their compositional, spatial, and functional properties, which is a significant step toward their deployment into functional nanoscale devices.

INTRODUCTION

30 The self-organization of macromolecular building blocks into 31 complex, functional systems is ubiquitous in nature. These 32 biomolecular assemblies serve as inspiration for the creation of 33 synthetic multicomponent materials that possess similar 34 degrees of spatial and chemical complexity. This concept 35 provides the intellectual underpinning for the emergent field of 36 nanoarchitectonics, in which nanomaterials with tailorable 37 structure and properties are engineered for real-world 38 applications. 1-3

Free-standing two-dimensional (2D) nanomaterials repre-40 sent an attractive class of synthetic targets within the 41 nanoarchitectonic field. The intrinsic physical properties 42 derived from their ultrathin construction coupled with the 43 ability to selectively functionalize the assembly surface give rise 44 to 2D substrates that have potential utility for a diverse set of 45 applications (e.g., biosensors, selectively permeable mem-46 branes, cell-instructive surfaces, biocatalytic and electronic 47 scaffolds, and material components for biomedical implants/ 48 devices).^{4–14} However, the vast majority of current methods

involving the bottom-up fabrication of 2D nanomaterials yield 49 heterogeneous distributions of assembled products with 50 limited compositional, spatial, and functional control. Con- 51 sequently, new synthesis protocols, in which one can 52 systematically tailor the chemical and physical properties of 53 2D nanostructures, are critical for realizing their potential 54

Recently, crystallization-driven seeded growth has been 56 developed as a method for the controlled fabrication of 2D 57 nanomaterials derived from organic and organometallic 58 polymers. 15-21 Although this method affords assemblies with 59 tailorable structure and composition, the scope of this seeded 60 growth process is, thus far, relatively limited. Expanding the 61 repertoire of programmable building blocks to encompass 62 peptides and proteins, which display a rich portfolio of 63 structure and function, would open the door for developing 64 new classes of functional 2D biomaterials. In contrast to 65

Received: August 28, 2019 Published: December 4, 2019

132

66 synthetic polymers, peptides and proteins display precisely 67 defined sequences, which can be configured to introduce 68 specific, directional interactions between subunits at the 69 nanoscale and thereby promote the formation of structurally 70 defined assemblies. Moreover, as precisely defined polymers of 71 biocompatible amino acids, their chemical composition bodes 72 well for the integration of the resultant materials with 73 biological systems.

Previously, we reported the fabrication of nanosheets 75 derived from collagen-mimetic peptides (CMPs). 22-24 CMP 76 sequences comprise a triblock architecture having three 77 sequential blocks of positively, neutral, and negatively charged 78 triads (Figure 1a). Upon folding, CMP triple helices assemble

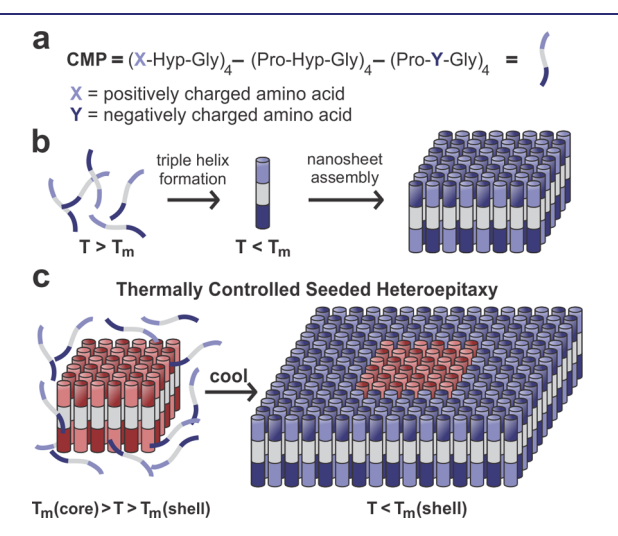


Figure 1. CMP nanosheet assembly. (a) Amino acid sequence of a CMP having triblock architecture with four neutral, positively, and negatively charged triad segments. (b) Folding of CMPs into collagen triple helices upon cooling the assembly solution below the triple helix $T_{\rm m}$ triggers their spontaneous assembly into a 2D lattice. CMP triple helices pack in an antiparallel fashion to facilitate favorable charge interactions between structurally adjacent triple helices. (c) At solution temperatures in which $T_{\rm m}({\rm core}) > T > T_{\rm m}({\rm shell})$, core nanosheet seeds (red) remain stable while shell CMPs (blue) are monomeric. Gradual cooling of the assembly solution to $T < T_{\rm m}({\rm shell})$ should lead to the formation of sectored core—shell nanosheets.

79 into a crystalline 2D lattice via Coulombic interactions 80 between oppositely charged residues on structurally adjacent 81 triple helices (Figure 1b). We have observed that for certain 82 CMPs the outcome of this self-assembly process is the 83 formation of structurally homogeneous nanosheets, in which 84 the nanosheet size and thermal stability depend on the 85 thermodynamic stability of the corresponding CMP triple 86 helix.²⁴ To ensure that self-assembly occurs via a controlled 87 process, CMP solutions are first heated to temperatures above 88 the melting temperature (T_m) of the corresponding nanosheet 89 to remove kinetically trapped intermediates that can result 90 from peptide synthesis and purification. Gradual cooling of 91 these solutions of monomeric CMPs to temperatures below 92 the triple helix $T_{\rm m}$ initiates the slow, controlled formation of 93 CMP triple helices, which triggers the spontaneous nucleation 94 and growth of 2D collagen nanocrystals.

The dependence of nanosheet formation on triple helix stability presents the opportunity to control the self-assembly process through manipulation of the solution temperature. Furthermore, we previously demonstrated that molecular 98 engineering of the CMP sequence enables control of the 99 triple helix $T_{\rm m}$ and the thermodynamic stability of the 100 corresponding nanosheets. ²⁴ These observations suggest that 101 CMP triple helices having different $T_{\rm m}$ values can be employed 102 to construct multicomponent core-shell nanosheets using a 103 temperature-controlled seeded growth assembly process. 104 Specifically, preformed nanosheets derived from CMPs 105 displaying higher thermal stability (i.e., higher triple helix $T_{\rm m}$ 106 values) can serve as crystalline templates for the thermally 107 controlled heteroepitaxial growth of CMP triple helices that 108 possess a lower melting transition. The key feature of this 109 process is that the assembly temperature can be maintained 110 such that $T_{\rm m}({\rm core}) > T > T_{\rm m}({\rm shell})$ (i.e., between the $T_{\rm m}$ of 111 both core and shell CMP triple helices). Under these 112 conditions, the shell peptide is in its monomeric form while 113 nanosheet seeds that comprise the core persist in the self- 114 assembled state (Figure 1c). We propose that gradually cooling 115 the solution to below the $T_{\rm m}$ of the shell CMPs should lead to 116 their controlled triple helix formation. The nascent triple 117 helices can deposit onto the lateral edges of the preexisting 118 core nanosheets via the same Coulombic interactions that 119 drive 2D self-assembly.

Herein, we present a versatile and straightforward strategy 121 for the design and synthesis of multicomponent 2D assembly 122 platforms using thermally controlled seeded growth assembly. 123 These resultant sectored nanosheets exhibit a core—shell 124 architecture in which each sector can be chemically and 125 structurally addressed. The present work establishes new 126 design and engineering principles for assembling multifunc- 127 tional, 2D biomolecular nanostructures that display composi- 128 tional, spatial, and functional control at the nanoscale, which is 129 a significant development within the realm of 2D nano- 130 architectonics.

■ RESULTS AND DISCUSSION

Independent Nanosheet Studies. Suitable CMP candi- 133 dates must possess differentiable thermal stabilities, as 134 determined from the $T_{\rm m}$ of the respective homomeric 135 assemblies, in order to effectively perform thermally controlled 136 heteroepitaxy. A previously studied CMP, $4S(X)_{444}$, assembles 137 into uniform nanosheets at 4 °C. 23,24 Its formation at low 138 temperature is attributed to the presence of noncanonical (2S, 139 4S)-4-aminoproline (amp; Figure 2a) residues in the Xaa 140 f2 position, which has been shown to destabilize the collagen 141 triple-helical structure.²⁵ With this in mind, we surmised that 142 incorporating a more sterically favorable analogue, (2S, 4R)-4- 143 aminoproline (Amp; Figure 2a), at homologous sites within 144 the peptide sequence would yield assemblies with greater 145 thermodynamic stability despite a similar macromolecular 146 architecture, thereby preserving the Coulombic interactions 147 that maintain the integrity of the 2D lattice. 25 We hypothesized 148 that assemblies of this peptide, termed $4R(X)_{444}$ (Figure 2a), 149 could serve as seeds for the epitaxial growth of $4S(X)_{444}$ triple 150 helices.

Initial studies were conducted to independently characterize 152 the properties of homogeneous nanosheets arising from the 153 self-assembly of the corresponding $4S(X)_{444}$ and $4R(X)_{444}$ 154 peptides. The purified CMPs (Figures S1 and S2) assemble 155 into well-defined nanosheets in MOPS buffer (pH 7.0) under 156 conditions in which the samples were heated to above the 157 individual $T_{\rm m}$ and then slowly cooled to the incubation 158 temperature (Figure S3). In the absence of thermolysis, ill- 159

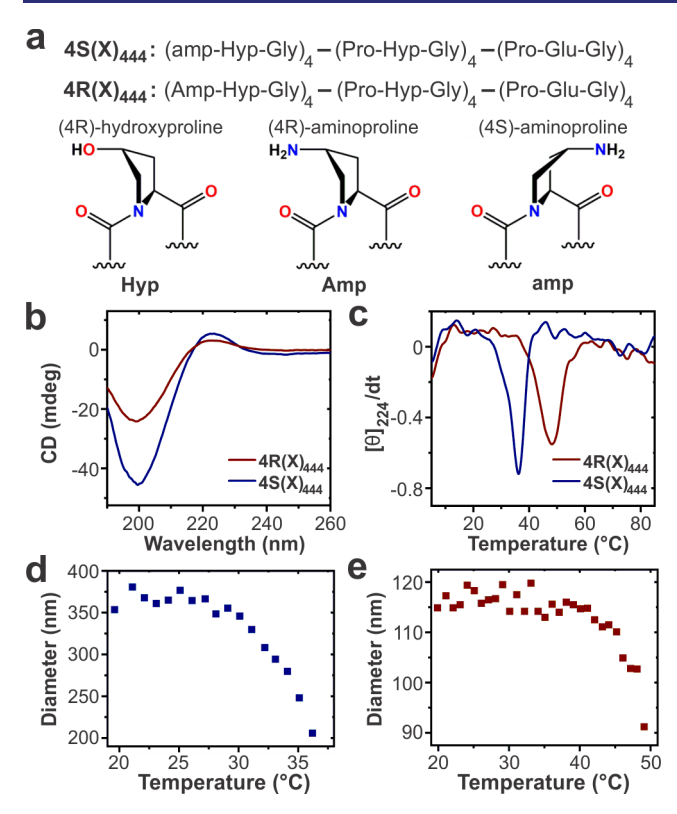


Figure 2. $4S(X)_{444}$ and $4R(X)_{444}$ nanosheet characterization. (a) Amino acid sequences of $4S(X)_{444}$ and $4R(X)_{444}$. Structures and ring pucker conformers of the incorporated imino acid derivatives are also shown. (b) CD spectra of $4S(X)_{444}$ and $4R(X)_{444}$ nanosheets. (c) First derivative of the CD signal at 224 nm as a function of temperature for $4S(X)_{444}$ (2 mg/mL) and $4R(X)_{444}$ (0.2 mg/mL) nanosheets. DLS melting curves of (d) $4S(X)_{444}$ and (e) $4R(X)_{444}$ nanosheets. All data were collected on nanosheets assembled after 2 weeks of incubation.

160 defined structures are observed, which validates the importance 161 of thermal annealing (Figure S4). Circular dichroism (CD) 162 spectropolarimetry of the nanosheets displays the characteristic profile of collagen triple helices, which is marked by maximum 164 and minimum peaks at 224 and 198 nm, respectively (Figure 165 2b). Importantly, as predicted, CD thermal denaturation 166 studies reveal triple-helical melting transition at 48 and 36 °C $167 (\Delta T_{\rm m} = 12 \, {}^{\circ}\text{C}) \text{ for } 4R(X)_{444} (0.2 \, \text{mg/mL}) \text{ and } 4S(X)_{444} (2.1 \, \text{mg/mL})$ 168 mg/mL) nanosheets, respectively (Figure 2c). It is important 169 to note that the $T_{\rm m}$ values pertain to triple helices within the 170 2D assembly. Previous studies have provided no evidence for 171 the formation of isolated triple helices (i.e., in the absence of 172 self-assembly into nanosheets).²⁴ The respective peptide 173 concentrations (0.2 and 2 mg/mL for $4R(X)_{444}$ and $4S(X)_{444}$, 174 respectively) reflect the optimized conditions employed in 175 subsequent seeded growth experiments (vide infra). These conditions provide more easily distinguishable shell growth, as 177 measured in terms of the change in nanosheet dimensions, which facilitates their characterization using microscopy

 regarding relative changes in nanosheet size in situ. A 187 significant decrease in particle size occurs at the respective 188 triple helix $T_{\rm m}$ of $4{\rm S}({\rm X})_{444}$ and $4{\rm R}({\rm X})_{444}$ nanosheets, 189 confirming the hypothesis that the triple helix is essential for 190 sheet integrity. The coincidence of the melting transition 191 observed from CD thermolysis experiments with a decrease in 192 the DLS scattering intensity reinforces the previously observed 193 notion that triple helix formation is a prerequisite for 194 nanosheet self-assembly.

Core—Shell Nanosheet Assemblies. Motivated by these 196 preliminary results, temperature-controlled seeded growth 197 experiments were performed (Figure 3a). A dilute solution 198 f3 of preassembled $4R(X)_{444}$ nanosheets (0.2 mg/mL) was 199 combined with $4S(X)_{444}$ (2 mg/mL). The mixture was heated 200 and held at 40 °C for 30 min. At this temperature and 201 concentration, $4R(X)_{444}$ nanosheet seeds persist in solution 202 ($T_{\rm m}=48$ °C), while $4S(X)_{444}$ is monomeric ($T_{\rm m}=36$ °C; 203 Figure S5). After 30 min, the solution was gradually cooled and 204 incubated at 4 °C. Substantially larger nanosheets (diagonal 205 length $L_{\rm d}=525\pm137$ nm) are observed after 11 days of 206 incubation (Figure 3b–d). These well-defined structures 207 sharply contrast with identical experiments that were 208 conducted without thermal input, which yielded polymorphic 209 and ill-defined products (Figure S6).

To confirm that these structures comprise distinct core and 211 shell domains, biotin-streptavidin bioconjugation was em- 212 ployed to probe the sheet surface. N-Terminal biotinylated 213 derivatives of $4S(X)_{444}$ and $4R(X)_{444}$ were synthesized and 214 purified (Figure S7). Because of the large size of streptavidin 215 $(\sim 4 \text{ nm})^{26}$ a small fraction of biotinylated peptide was 216 deemed sufficient for the saturation of the sheet surface. 217 Biotin-doped (5%) $4R(X)_{444}$ (b- $4R(X)_{444}$) assembles into 218 nanosheets of comparable size with respect to their pure 219 $4R(X)_{444}$ counterpart ($L_d = 149 \pm 47$ nm, Figure S8a,b). The 220 lack of a detectable change in $T_{\rm m}$ implies that the presence of 221 biotin has no observable effect on the triple helix stability 222 (Figure S8c). As previously observed, seeded growth experi- 223 ments yield larger sheets with dimensions similar to those of 224 $4R(X)_{444} @ 4S(X)_{444}$ (core@shell) nanosheets ($L_d = 562 \pm 87$ 225 nm, Figure S9). Atomic force microscopy (AFM) analysis, 226 after streptavidin addition, confirms the core-shell architec- 227 ture (Figures 3f and S10).

Further analysis of the AFM data determined that diblock 229 assemblies account for $\sim 85\%$ of the product distribution with 230 the remaining $\sim 15\%$ representing self-nucleated $4S(X)_{444}$ 231 nanosheets, which indicates that $4S(X)_{444}$ triple helices favor 232 epitaxial growth over self-nucleation. 24 Although representing a 233 minor product, the formation of pure $4S(X)_{444}$ nanosheets 234 highlights the importance of employing CMP triple helices that 235 exhibit slow nanosheet nucleation kinetics. Analogous experiments, conducted on $4R(X)_{444}@b-4S(X)_{444}$ sheets, yield 237 similar results (Figures 3g and S11 and S12). Height traces 238 measured across the center of streptavidin-coated sheets show 239 distinct height differences of ~ 4 nm, indicating the successful 240 site-specific immobilization of streptavidin (Figure 3e–g).

Synchrotron small-angle/wide-angle X-ray scattering 242 (SAXS/WAXS) experiments were carried out to characterize 243 the internal structure of $4R(X)_{444}@4S(X)_{444}$ nanosheets. To 244 discern whether the distinct peptide domains maintain their 245 intrinsic lattice parameters, homomeric $4R(X)_{444}$ and $4S(X)_{444}$ 246 nanosheets were also studied. Scattering curves of all three 247 CMP assembly solutions verify a similar underlying structure 248 (Figure 3h). Form-factor scattering intensities in the low-q 249

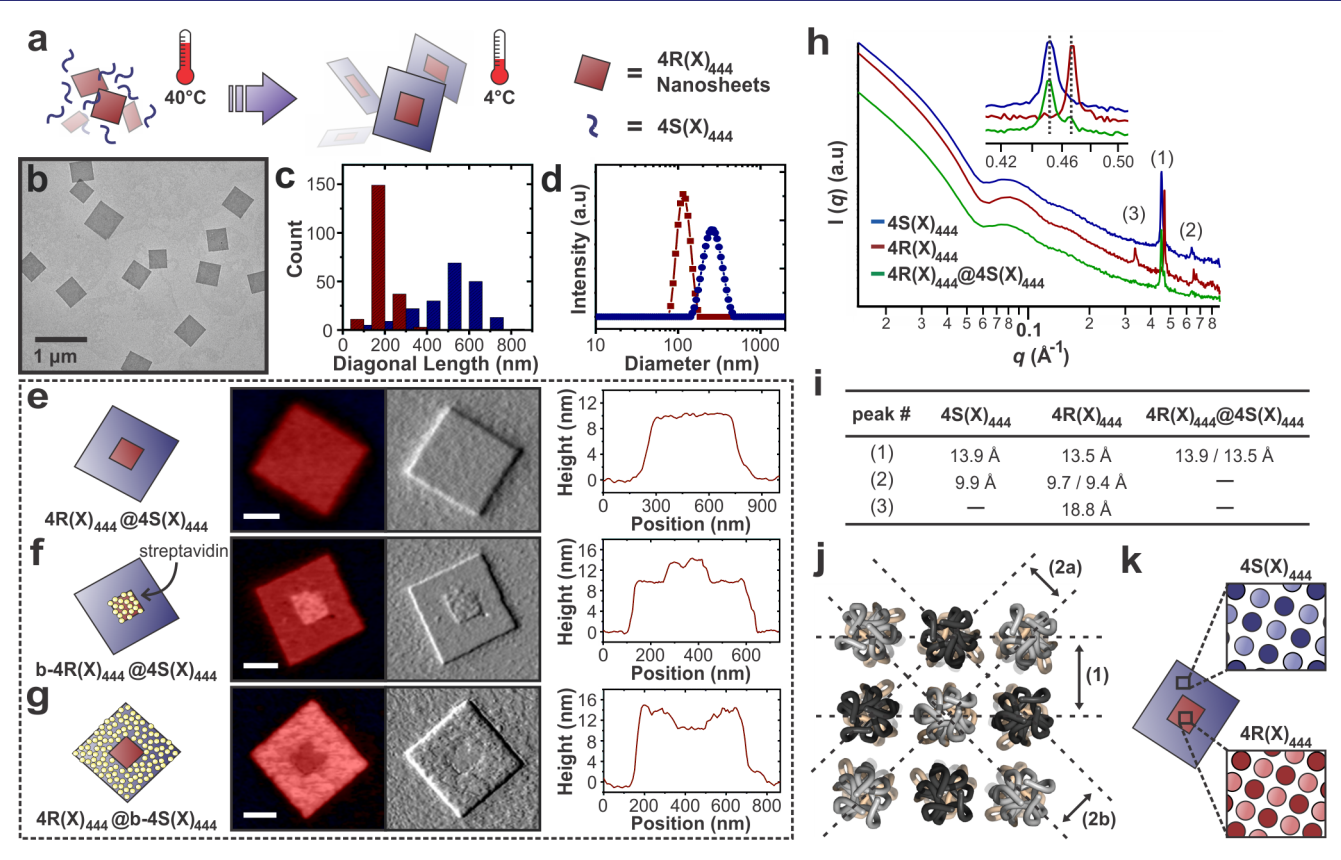


Figure 3. Core—shell nanosheet assembly and characterization. (a) Scheme detailing the assembly of $4R(X)_{444}@4S(X)_{444}$ nanosheets via thermally controlled seeded growth. (b) Stained TEM image of $4R(X)_{444}@4S(X)_{444}$ nanosheets after 11 days of assembly time. (c) Diagonal length distribution of $4R(X)_{444}$ nanosheet seeds (red bars, 163 ± 49 nm, based on 200 counts) and $4R(X)_{444}@4S(X)_{444}$ nanosheets (blue bars, 525 ± 137 nm, based on 200 counts) after 2 weeks and 11 days of assembly time, respectively. (d) DLS spectra of $4R(X)_{444}$ nanosheet seeds (red line) and $4R(X)_{444}@4S(X)_{444}$ nanosheets (blue line). AFM data (left to right: core—shell nanosheet model; height image (scale bar = 200 nm), amplitude image, and height profile across the center of the core—shell nanosheet) for (e) $4R(X)_{444}@4S(X)_{444}$, (f) streptavidin-coated $4R(X)_{444}@b-4S(X)_{444}$ nanosheets. (h) Synchrotron SAXS scattering profile of $4S(X)_{444}$, $4R(X)_{444}$, and $4R(X)_{444}@4S(X)_{444}$ nanosheets and (i) corresponding d-spacing values associated with peaks (1), (2), and (3). (j) Assembly packing model of collagen triple helices ordered into a 2D tetragonal lattice. Gray and black coloring highlights the antiparallel packing between adjacent triple helices. (k) Two structurally distinct lattices are present within $4R(X)_{444}@4S(X)_{444}$ nanosheets.

250 region ($q < 0.02 \text{ Å}^{-1}$) roughly follow a q^{-2} power law, 251 indicating sheetlike morphology for all CMP nanosheets. 252 Fitting the low-q data using the Guinier equation for the 253 sheetlike form indicates similar average sheet thicknesses that 254 are consistent with AFM and theoretical height calculations 255 (109.6, 105.9, and 106.1 Å for $4R(X)_{444}$, $4S(X)_{444}$, and 256 $4R(X)_{444}@4S(X)_{444}$ nanosheets, respectively; Figures 3e and 257 S13). The oscillations in the q range of $\sim 0.04-0.2 \text{ Å}^{-1}$ stem 258 from the thickness of the nanosheets, and its attenuation 259 reflects the variation in sheet thickness.

Bragg diffraction peaks in the high-q region of the intensity 261 plot indicate a high degree of crystallinity within the 2D 262 assemblies (Figure 3h,i). Peaks (1) and (2) constitute the 263 triple helix packing parameters, where the former corresponds 264 to distances between [1, 0] or [0, 1] planes (d_{helix}) and the 265 latter corresponds to distances between [1, 1] planes (Figure 266 3j). A Calculated d spacings of 13.9 and 9.9 Å for peaks (1) and 267 (2), respectively, for d(X) and 268 arrangement of triple helices (9.9 Å × d(2) ≈ 14 Å). In 269 contrast, the d(helix) for d(X) and 9.4 Å (Figure S14). The presence of 272 both peaks (corresponding to 2a and 2b in Figure 3j) implies 273 that the tetragonal lattice is slightly distorted. Moreover, a third

peak, designated as peak (3), may represent a higher-order [1, 274 1] plane (9.4 Å \times 2 = 18.8 Å) within the 4R(X)₄₄₄ lattice. To 275 summarize, the 4R(X)₄₄₄ lattice is slightly more contracted and 276 distorted than its 4S(X)₄₄₄ counterpart.

Interestingly, two sets of peaks are observed for $4R(X)_{444}$ @ 278 $4S(X)_{444}$ nanosheets (Figure 3h inset). Their associated $d_{\rm helix}$ 279 values, which correspond to the respective lattice parameters 280 for the individual components, indicate that the core and shell 281 domains retain their inherent packing structure (Figure 3k). 282 This observation is not too surprising considering that the 283 calculated lattice mismatch is approximately 3% ((13.5 Å – 284 13.9 Å)/13.5 Å), which is well below the benchmark limit of 285 15% for the successful heteroepitaxy of polymers. 16,27 The 286 epitaxial growth of $4S(X)_{444}$ onto $4R(X)_{444}$ seed templates can 287 therefore, in part, be credited to the structurally similar lattices 288 of both components. These results differ from previous work 289 with block copolymers in which the core lattice structure was 290 maintained throughout the shell layer. 16

High-Resolution Cryo-TEM Analysis. Cryogenic trans- 292 mission electron microscopy (cryo-TEM) was employed to 293 examine the heteroepitaxial interface. Because of the high 294 throughput afforded by automated data collection, the analysis 295 of hundreds of nanocrystals afforded a yield of 87% diblock 296 assemblies and 13% single-block assemblies (n = 463), which 297

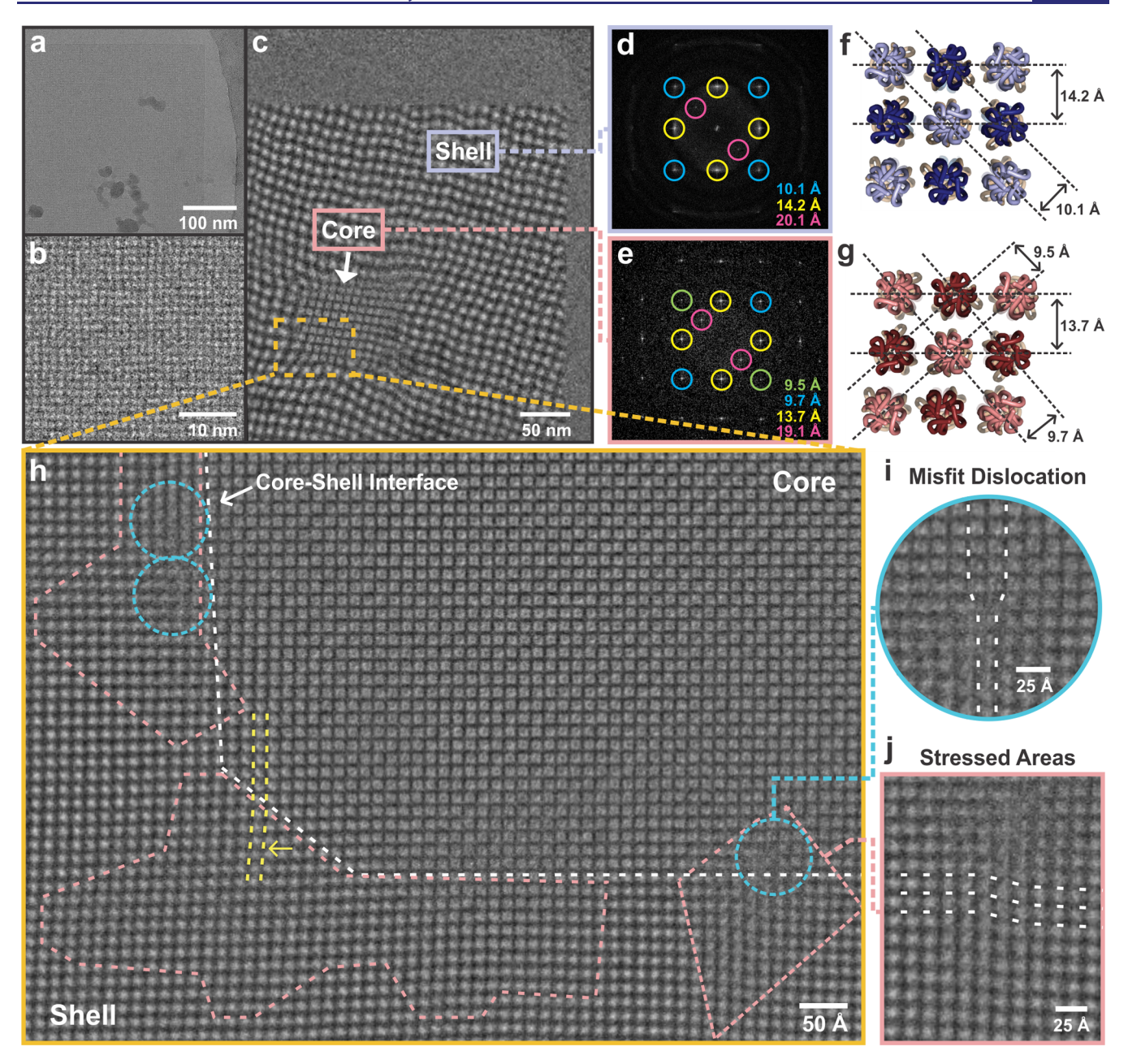


Figure 4. High-resolution cryo-TEM analysis. (a) Cryo-TEM image of a $4R(X)_{444}$ @ $4S(X)_{444}$ nanosheet. (b) Enlarged image of the $4R(X)_{444}$ @ $4S(X)_{444}$ nanosheet reveals the tetragonal arrangement of CMP triple helices comprising the 2D lattice. (c) Moiré evaluation conducted on a $4R(X)_{444}$ @ $4S(X)_{444}$ nanosheet confirms the presence of the core and shell sectors within the assembly. FFT analysis of the (d) shell and (e) core region of $4R(X)_{444}$ @ $4S(X)_{444}$ nanosheets. Proposed triple helix packing model of (f) the $4S(X)_{444}$ shell and (g) the $4R(X)_{444}$ core (d spacings obtained from FFTs). (h) Overlay of the filtered cryo-TEM image over the original drift-corrected image showing the core—shell interface (white dashed line) and the various mechanisms employed by the nanocrystal to alleviate strain associated with the interfacial lattice mismatch. Dashed blue circles indicate misfit dislocation sites, and dashed pink boxes indicate stressed areas as defined by the bending of the triple-helical rows (e.g., yellow dashed lines; arrow indicates the bending direction) and areas where the triple helices are less resolved. Enlarged image of (i) a misfit dislocation site and (j) a stressed area.

²⁹⁸ agree with the results acquired from AFM analysis (Figure ²⁹⁹ S15). High-resolution images of $4R(X)_{444}@4S(X)_{444}$ reveal ³⁰⁰ the ordered organization of individual triple-helical protomers ³⁰¹ within the 2D lattice (Figure 4a,b). To visualize the core and ³⁰² shell sectors, a Moiré evaluation was used in which a fixed ³⁰³ raster was applied over the image while decreasing the image ³⁰⁴ size (i.e., under sampling). At a given image scaling, the raster ³⁰⁵ creates Moiré patterns, which provides visual evidence of the ³⁰⁶ two sectors (Figure 4c). ²⁸

Fast Fourier transforms (FFTs) of cryo-TEM micrographs $_{307}$ confirm the presence of two unique tetragonal lattices as $_{308}$ evidenced by two distinct sets of Bragg spots that exhibit 4-fold $_{309}$ rotational symmetry (Figure S16). Selected area FFTs of the $_{310}$ shell and core regions were analyzed to determine the lattice $_{311}$ packing parameters (Figure 4d,e). Sharp Bragg spots, $_{312}$ associated with d spacings within the $4R(X)_{444}$ lattice, extend $_{313}$ to a resolution of ~ 3.8 Å, indicating a highly ordered core $_{314}$ (Figure S17). FFTs of the $4S(X)_{444}$ shell yields less-well- $_{315}$ defined Bragg spots with corresponding d spacings limited to $_{316}$

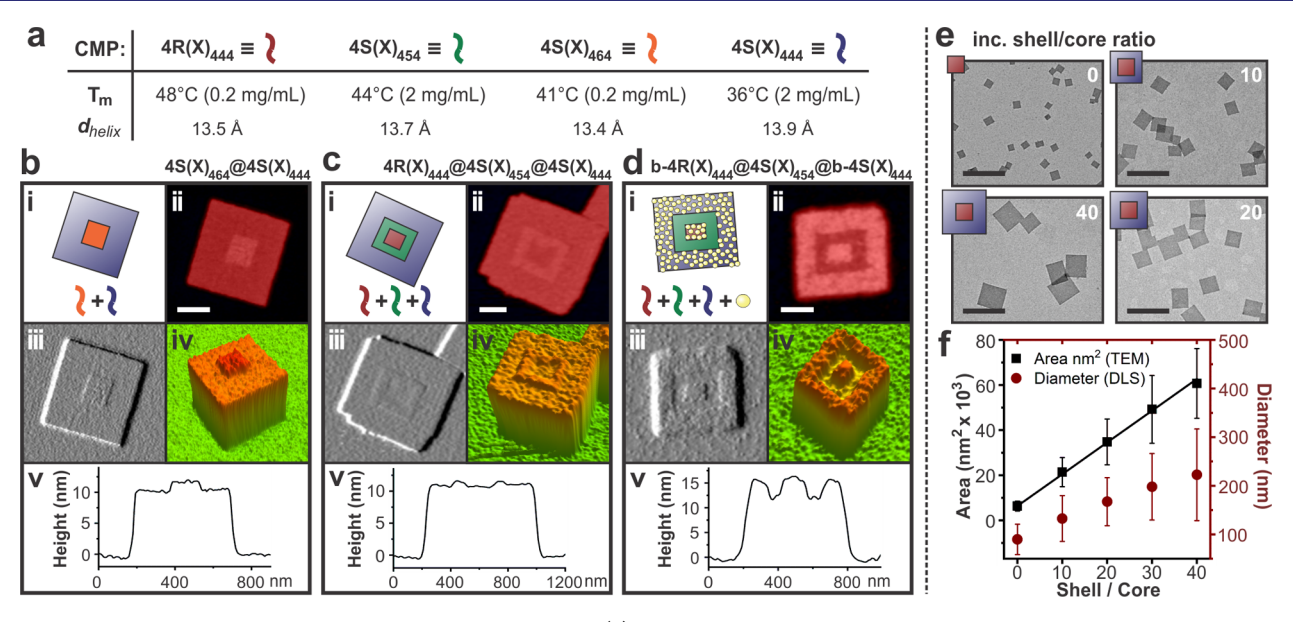


Figure 5. Compositional and size control of sectored nanosheets. (a) Various CMPs employed for assembling diblock and triblock nanosheet architectures with corresponding $T_{\rm m}$ and $d_{\rm helix}$ values obtained from SAXS ($d_{\rm helix}$ values for $4S(X)_{454}$ and $4S(X)_{464}$ were obtained from ref 24). AFM data [(i) nanosheet assembly model, (ii) height image, (iii) amplitude image, (iv) 3D reconstruction, and (v) height profile across the nanosheet center] of (b) $4S(X)_{464} @4S(X)_{444}$, (c) $4R(X)_{444} @4S(X)_{454} @4S(X)_{444}$, and (d) $b-4R(X)_{444} @4S(X)_{454} @b-4S(X)_{444}$ nanosheets (scale bars = 200 nm). (e) Stained TEM images of $4R(X)_{444} @4S(X)_{444}$ nanosheets assembled under basic conditions (pH 8.0) at various shell/core ratios (scale bars = 500 nm). (f) Linear dependence of the nanosheet area, calculated from TEM images (black line), and corresponding hydrodynamic average diameters, obtained from DLS, as a function of the shell/core ratio (error bars represent a single standard deviation).

 $_{317}$ ~6.4 Å, implying that the $4S(X)_{444}$ triple-helical framework is $_{318}$ less ordered (Figure S18). Measured d spacings of the shell $_{319}$ (14.2 and 10.1 Å) and core (13.7, 9.7, 9.5, and 19.1 Å) agree $_{320}$ with values obtained from SAXS and define the d spacings $_{321}$ within the triple helix packing models (Figure 4f,g).

Heteroepitaxial growth often introduces crystalline defects that arise from the necessity to alleviate elastic strain associated with the lattice mismatch. Although this phenomenon has been studied extensively for inorganic- and polymer-based systems, heteroepitaxial interfaces within crystalline biological materials have not been fully characterized. We therefore conducted a detailed analysis of the core—shell interface, which revealed several structural distortions within the triple helix packing (Figure 4h). First, misfit dislocations are observed at sites along the core—shell border (Figure 4i). Such defects are common at the heteroepitaxial boundary arising from differsidences in lattice parameters between the substrate (core) and growth (shell) layers.

In addition to dislocations, the presence of stressed areas is 335 336 commonly observed, which correspond to visually distinguishable areas in which triple helices are less well-resolved and in 337 which triple helix packing is angularly distorted (e.g., bending of triple-helical rows; Figure 4h,j). We hypothesize that these stressed regions develop as a compensation mechanism in which elastic strain stemming from lattice mismatch at the core-shell interface locally overcomes the electrostatic interactions that determine the symmetry of triple helix packing. This interfacial compliance may be attributable to the deformable nature of $4S(X)_{444}$ triple helices and the 346 relatively weak cohesive interactions between them, both of which may account for a lattice that can be more easily 348 distorted to accommodate lattice strain.³

The various degrees of strain within the shell sector are sector are sector in multiple regions within the sector are sec

a greater degree of disorder (as defined by a lack of sharpness $_{352}$ of Bragg spots) compared to FFTs collected at positions near $_{353}$ the sheet periphery, signifying that the $_{45}(X)_{444}$ lattice near $_{354}$ the heteroepitaxial interface is subjected to a greater amount of $_{355}$ strain (Figure S19). Finally, FFT analysis reveals a slight $_{356}$ discrepancy between the orientation of the core and shell $_{357}$ lattice (up to $_{\sim}1.2^{\circ}$), which suggests that the $_{45}(X)_{444}$ $_{358}$ assembly lattice self-configures, presumably to improve alignary ment with the core lattice template (Figure S20).

In conclusion, these results demonstrate that the less 361 thermodynamically stable $4S(X)_{444}$ triple helices are tasked 362 with absorbing the interfacial strain created at the hetero- 363 epitaxial interface. The apparent malleability of the softer 364 $4S(X)_{444}$ triple helix lattice, as determined by the significant 365 presence of stressed areas, contrasts with that of rigid lattice 366 materials (e.g., ionic solids and metals) which comprise atoms 367 that behave as "hard spheres". 31 It is important to note that 368 although the collagen-based structures are relatively pliable, 369 dislocations are still required to relieve elastic strain at the 370 core-shell interface, akin to traditional inorganic materials. 371 These findings afford a new level of understanding of the 372 mechanisms that underlie the heteroepitaxial growth of soft, 373 biological structural units. We envision that these foundational 374 insights will serve as a starting point for engineering 375 multicomponent, multidomain assemblies from crystallizable 376 biomolecules.

Compositional and Size Control. We hypothesized that 378 a diverse collection of sectored nanosheets could be 379 constructed if a wider range of CMPs were identified that 380 met a specific set of structural criteria. We posit that the 381 individual components should exhibit (1) a sufficient differ- 382 ence in thermodynamic stability ($\Delta T_{\rm m}$); (2) a comparable 383 degree of cohesive electrostatic interactions between oppo- 384 sitely charged blocks; and (3) similar lattice packing 385 parameters. Although initial studies focused on alterations to 386

387 the amino acid sequence (amp vs Amp) to establish an 388 effective $\Delta T_{\rm m}$, a reasonable alternative approach would be to 389 vary the CMP length. Increasing the number of Pro-Hyp-Gly 390 triads has been demonstrated to increase the thermodynamic 391 stability of collagen triple helices and their assembled 392 structures. ^{24,32} Although this may decrease the number of 393 electrostatic interactions at the core—shell interface, we 394 anticipated that if a sufficient number of interactions are 395 maintained, this perturbation would have a minimal effect on 396 their coassembly.

To test this hypothesis, we employed nanosheets derived 398 from $4S(X)_{464}$, which comprise two additional Pro-Hyp-Gly 399 triads within the central block, to serve as seeds for the 400 templated growth of $4S(X)_{444}$. $4S(X)_{464}$ assembles into small 401 nanosheets with a $T_{\rm m}$ of 41 °C (0.2 mg/mL; Figures S21 and 402 S22). Upon addition of $4S(X)_{444}$, larger nanosheets are 403 observed after 2 weeks (Figure S21). AFM analysis of 404 $4S(X)_{464}$ @ $4S(X)_{444}$ nanosheets reveals a greater height for 405 the central core of the resultant assemblies (Figures Sb and 406 S23). A height difference of ~1 nm across the center of the 407 nanosheet is consistent with the approximate length of a single 408 Pro-Hyp-Gly triad (0.286 nm rise/residue). 33,34 We propose 409 that longer $4S(X)_{464}$ triple helices protrude from both faces of 410 the nanosheet, as would be expected for antiparallel triple helix 411 packing (Figure Sb). 35

This seeded growth process should be relatively straightfor-413 ward to extend to triple-sector assemblies if three triple-helical 414 protomers could be identified that possess significant $T_{
m m}$ 415 differences in the order $T_{\rm m}({\rm core}) > T_{\rm m}({\rm shell_1}) > T_{\rm m}({\rm shell_2})$ 416 (Figure 5a). Initial attempts to construct $4R(X)_{444} @ 4S$ -417 $(X)_{464}$ @4S $(X)_{444}$ nanosheets were unsuccessful because of 418 the competitive self-nucleation of $4S(X)_{464}$, highlighting again 419 the importance of selecting CMPs in which self-nucleation is 420 slower than epitaxial growth. Subsequent attempts employing 421 **4S**(**X**)₄₅₄ (2 mg/mL, $T_{\rm m}$ = 44 °C; Figure S24) as the middle 422 layer proved to be more successful. AFM images of $4R(X)_{444}$ @ 423 $4S(X)_{454}$ diblock assemblies reveal heteroepitaxial growth with 424 few self-nucleated $4S(X)_{454}$ nanosheets (Figure S25). $4S(X)_{444}$ 425 was introduced into these diblock structures, and the solution 426 was heated to 38 °C (in between the $T_{\rm m}$ of $4{\rm S}({\rm X})_{454}$ and 427 $4S(X)_{444}$ triple helices) and then gradually cooled to 4 °C. An 428 AFM analysis of $4R(X)_{444}@4S(X)_{454}@4S(X)_{444}$ nanosheets 429 resolved the triblock assembly architecture (Figures 5c and 430 S26). A biotinylated derivative of the sectored triblock 431 assembly $(b-4R(X)_{444}@4S(X)_{454}@b-4S(X)_{444})$ was also syn-432 thesized, in which the core and outermost sectors were 433 functionalized. The site-specific deposition of streptavidin onto 434 the nanosheets generates a square bull's-eye pattern, which demonstrates the selective labeling of the sheet surface 436 afforded by compositionally tuning each sector (Figures 5d 437 and S27).

Seeded growth methods permit rational control over 439 assembly dimensions because they minimizes the lag phase 440 that can result in competitive self-nucleation. 15,19,36,37 The 441 large-scale production of nanosheets with specific uniform sizes 442 is important for bringing these 2D materials from the benchtop 443 to the marketplace. However, uniform core—shell architec-444 tures require the availability of uniform populations of seeds 445 that can serve as templates. Through systematic studies, we 446 determined that $4R(X)_{444}$ assembles into small, monodisperse 447 nanosheets ($L_d = 106 \pm 19$ nm) under slightly basic conditions 448 (pH 8.0; Figure S28). We speculate that electrostatic 449 interactions between triple-helical protomers are weakened at

higher pH, which limits the lateral growth of the resultant $_{450}$ nanosheets. The triple helices are slightly destabilized ($T_{\rm m}=42$ $_{451}$ °C, 0.2 mg/mL; Figure S29) compared to sheets grown at $_{452}$ neutral pH. With seeds in hand, a systematic adjustment of the $_{453}$ amount of shell peptide to core peptide ("shell/core ratio") $_{454}$ tunes the nanosheet size across the mesoscale regime with an $_{455}$ apparently linear dependence (Figures 5e,f and S30 and S31). $_{456}$ We note that in the absence of seeds, $_{45}$ (X) $_{444}$ still form $_{457}$ nanosheets under basic conditions ($T_{\rm m}=30$ °C, 2 mg/mL) $_{458}$ but exhibits no linear size dependence (Figure S32).

Surface Functionalization. Multiple peptide sectors 460 within a single nanosheet offers the potential for fabricating 461 multifunctional 2D platforms in which each sector can be 462 individually addressed through selective chemical modification. 463 As a proof-of-concept, a dual-binding assembly platform was 464 constructed in which N-terminal-modified biotin and azide 465 CMP derivatives (N3-4R(X)₄₄₄, Figure S33) were incorpotated into the core and shell sectors, respectively. To visualize 467 the site-specific binding on the sheet surface, Cy3B and AF647 468 fluorophores were employed as probes (Figure 6a). We note 469 for that larger, more polydisperse 4R(X)₄₄₄ seeds (nanosheets 470 grown at 2 mg/mL) were used to allow for improved 471

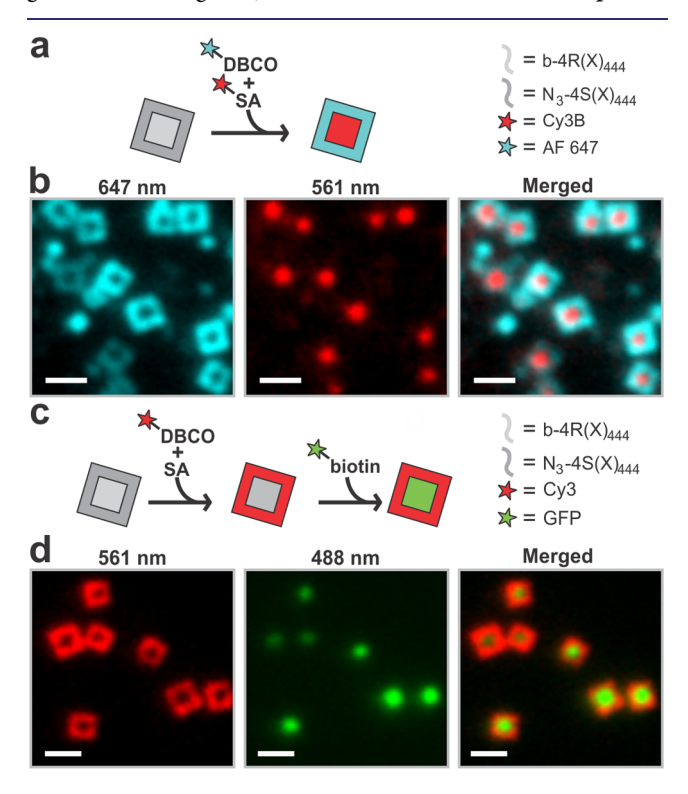


Figure 6. Surface functionalization. (a) Scheme detailing the site-specific attachment of DBCO-AF647 and SA-Cy3B onto b-4R(X)₄₄₄@N₃-4S(X)₄₄₄ nanosheets (SA = streptavidin). (b) Fluorescence optical micrographs of b-4R(X)₄₄₄@N₃-4S(X)₄₄₄ nanosheets functionalized with AF647 and Cy3B at various emission wavelengths. The observed fluorescence emissions recapitulate the core—shell assembly architecture (scale bar = 2 μ m). (c) Scheme detailing the two-step site-specific attachment of DBCO-Cy3 and biotin-GFP onto b-4R(X)₄₄₄@N₃-4S(X)₄₄₄ nanosheets. (d) Fluorescence optical micrographs of b-4R(X)₄₄₄@N₃-4S(X)₄₄₄ nanosheets functionalized with Cy3 and GFP at various emission wavelengths (scale bar = 2 μ m). False color was used for AF647 fluorescence to enhance the contrast.

472 visualization using fluorescence optical microscopy (Figure 473 S34a).

A solution of $b-4R(X)_{444}@N3-4S(X)_{444}$ nanosheets prepared via conventional seeded growth (Figure S34b) was incubated overnight at 4 °C with streptavidin-tagged Cy3B and DBCO-tagged AF647 (DBCO = dibenzocyclooctyne). After the removal of excess dye, fluorescence optical microscopy experiments confirmed the successful dual-functionalization of $b-4R(X)_{444}@N3-4S(X)_{444}$ nanosheets. Cy3B fluorescent emission localizes within the core, while the AF647 fluorescence appears in the shell (Figure 6b).

Motivated by the robust, interchangeable platform accessible using bioorthogonal conjugation methods, a two-step protocol was employed to immobilize biotinylated green fluorescent fluorescent (GFP) and Cy3 to the nanosheet core and shell, respectively (Figure 6c). Fluorescence optical micrographs confirm that the respective molecular labels segregate to the sector that is functionalized with the complementary chemical for these architecturally defined nanostructures for patterning biologically/chemically relevant cargo onto a 2D scaffold with nanoscale spatial specificity.

494 CONCLUSION

495 We present a general methodology for designing and 496 constructing structurally and chemically tailorable 2D crystal-497 line nanostructures, which comprise rationally engineered 498 CMP sectors that coassemble via temperature-controlled 499 heteroepitaxy. These nanosheets are composed of distinct 500 CMPs that can be selectively functionalized within definable 501 spatial regions on the nanosheet surface using bioorthogonal 502 and biocompatible affinity binding or covalent capture. 503 Furthermore, cryo-TEM bestows an unprecedented degree of 504 insight into heteroepitaxial growth processes within the context 505 of biological soft materials. The observed lattice dislocations 506 and distortions are a consequence of the core-shell structures 507 we describe, in view of the incompatible lattice parameters of 508 the core and shell domains. These imperfections confirm a 509 malleability of ordered soft matter, which is not encountered 510 commonly in other systems. These lattice defects may allow an 511 alternative type of specific functionalization of the core-shell 512 structures at the defect sites (e.g., by introducing alternative 513 components that stabilize the lattice by binding to or inserting 514 into its defects). The present work represents an advancement 515 in developing 2D nanomaterials with nano- to mesoscale 516 structural and functional control via bottom-up solution-phase 517 assembly methods.

8 EXPERIMENTAL METHODS

Materials and Methods. Chemical reagents were purchased from S20 Sigma-Aldrich Chemical Co. (St. Louis, MO) and used without S21 further purification. Fmoc-Gly-HMP-TentaGel resins were purchased S22 from Anaspec (Fremont, CA). Boc-(2S, 4S)-4-amino-1-Fmoc-S23 pyrrolidine-2-carboxylic acid and Boc-(2S, 4R)-4-amino-1-Fmoc-S24 pyrrolidine-2-carboxylic acid were purchased from Chemimpex S25 (Wood Dale, IL). Biotin-PEG2-acid and azido-PEG5-acid were purchased from Broadpharm (San Diego, CA). DBCO-Cy3 and S27 DBCO-AF647 were purchased from Click Chemistry Tools S28 (Scottsdale, AZ). Biotin-GFP was purchased from ProteinMods S29 (Madison, WI). Peptides were quantified by mass and dissolved in S30 water, followed by separation into aliquots of known amounts of s31 peptides and lyophilization. Matrix-assisted laser desorption ionization S32 time-of-flight mass spectrometry (MALDI-TOF) data were collected S33 using an Applied Biosystem 4700 mass spectrometer (positive

reflector mode; accelerating voltage 20 kV) and using α -cyano-4-534 hydroxycinnamic acid (CHCA) as the ionization matrix. Diagonal 535 lengths of nanosheets were measured using *ImageJ*. 536

Peptide Synthesis and Purification. Peptides were prepared 537 using microwave-assisted synthesis on a CEM Liberty solid-phase 538 peptide synthesizer and Fmoc-Gly-HMP-Tentagel resin. Standard 539 Fmoc protection chemistry was employed with coupling cycles based 540 on HBTU/DIEA-mediated activation protocols and base-induced 541 deprotection (20% piperidine in DMF) of the Fmoc group. For 542 biotinylated and azide-modified peptides, biotin-PEG2-acid and 543 azido-PEG5-acid were used to cap the N-terminus of the peptide 544 while the peptide was still attached to the resin (no final deprotection 545 step). After coupling, the DMF/resin mixture was filtered and rinsed 546 with acetone and then air-dried. The crude peptides were cleaved for 547 3 h with a cleavage solution consisting of 92.5% TFA/2.5% H₂O/ 548 2.5% DODT/2.5% TIS (TFA = trifluoroacetic acid, DODT = 3,6-549 dioxa-1,8-octane-dithiol, TIS = triisopropylsilane). After filtration, the 550 crude peptide product in TFA was precipitated with cold Et₂O and 551 centrifuged at 4 °C. The supernatants were discarded, and the pellets 552 were dried under vacuum overnight.

Crude peptides were purified using a Shimadzu LC-20AP reverse- 554 phase high-performance liquid chromatography (HPLC) instrument 555 equipped with a preparative scale C18 column. Peptides were eluted 556 with a linear gradient of water—acetonitrile with 0.1% trifluoroacetic 557 acid (TFA). The target fractions were collected and lyophilized. The 558 lyophilized peptide was repurified via HPLC under the same protocol 559 described above and lyophilized. Doubly pure peptides were dialyzed 560 against HPLC-grade $\rm H_2O$ to remove residual TFA (MWCO = 2000 561 Da). The resulting peptide solutions were lyophilized once more and 562 stored at $\rm -30~^{\circ}C$.

Sectored Nanosheet Assembly Experiments. Annealing 564 experiments were conducted using a Fisher T-100 thermal cycler. 565 Single-component nanosheets were dissolved in 20 mM 3-(*N*- 566 morpholino)propanesulfonic acid (MOPS) buffer (pH 7.0) or *N*- 567 [tris(hydroxymethyl)methyl]-3-aminopropanesulfonic acid (TAPS) 568 buffer (pH 8.0) and held at 90 °C for 15 min and then cooled to 569 25 or 4 °C (0.5 °C/2.5 min rate). The sheets were allowed to 570 assemble for 2 weeks.

Heteroepitaxial growth experiments were conducted by adding a 572 solution of preformed nanosheet seeds (in either 20 mM MOPS 573 buffer, pH 7.0, or 20 mM TAPS buffer, pH 8.0) to lyophilized shell 574 peptide. The final CMP concentrations of both components were 575 ensured by diluting a 1 mg/mL stock solution of nanosheet seeds and 576 varying the amount of lyophilized shell peptide added to the seed 577 solution. The peptide mixture was then held at temperatures between 578 the $T_{\rm m}$'s of both CMPs for 30 min, except when constructing 579 $4R(X)_{444}@4S(X)_{454}$ nanosheets (hold time = 3 min). The holding 580 temperatures varied depending on the CMPs employed: $4R(X)_{444}@4S(X)_{454}$ 581 $4S(X)_{444}=40$ °C; $4S(X)_{446}@4S(X)_{454}@4S(X)_{444}=38$ °C. After the hold 583 time was completed, the solutions were cooled (0.5 °C/2.5 min) to 584 room temperature $(4R(X)_{444}@4S(X)_{454})$ or 4 °C $(4R(X)_{444}@4S(X)_{444})$ 585 $4S(X)_{444}$ $4S(X)_{464}@4S(X)_{444}$ and $4R(X)_{444}@4S(X)_{454}@4S(X)_{444}$. 586 $4S(X)_{444}$ $4S(X)_{464}@4S(X)_{444}$ and $4R(X)_{444}@4S(X)_{454}@4S(X)_{444}$. 586

Dual-Functionalization Experiments. For the AF647/Cy3B s87 system, DBCO-AF647 (1.5 μ L, 1 mg/mL solution in water) and s88 Cy3B-SA (2 μ L, 1 mg/mL solution in water) were added to a 35 μ L s89 solution of **b-4R(X)**₄₄₄@N3-4S(X)₄₄₄ nanosheets (2.2 mg/mL). The s90 mixture was incubated for 1 h at room temperature in the dark and s91 then placed in the refrigerator overnight (4 °C). The next day, the s92 solution was centrifuged at 3500g for 10 min. The supernatant was s93 removed and replaced with fresh 20 mM MOPS buffer (pH 7.0), and s94 the sample was vortex mixed.

For the GFP/Cy3 system, DBCO-Cy3 (0.5 μ L, 1 mg/mL solution 596 in water) and streptavidin solution (1 μ L, 1 mg/mL solution in water) 597 were added to 15 μ L of a solution of **b**-4**R**(X)₄₄₄@N3-4**S**(X)₄₄₄ 598 nanosheets (2.2 mg/mL). The mixture was incubated for 1 h at room 599 temperature in the dark. After 1 h, biotin-GFP (1 μ L, 1.5 mg/mL) 600 was added to the assembly solution. The solution was then placed in 601 the refrigerator overnight. The next day, the solution was centrifuged 602 at 3000g for 10 min. The supernatant was removed and replaced with 603

710

711

716

724

725

604 fresh 20 mM MOPS buffer (pH 7.0), and the sample was vortex 605 mixed.

Gircular Dichroism Spectroscopy. CD measurements were conducted on a Jasco J-810 CD spectrometer. Three spectra were recorded and averaged from 260 to 190 nm at a scanning rate of 100 nm/min and a bandwidth of 2 nm. CD melting experiments were performed in the temperature range from 5 to 85 °C at a heating rate of 20 °C/h. The intensity of the CD signal at 224 nm was monitored as a function of temperature.

Transmission Electron Microscopy. TEM images were collected with a Hitachi H-7700 transmission electron microscope at an accelerating voltage of 80 kV. TEM specimens were prepared by briefly mixing 2.5 μ L of peptide nanosheet solution with 2.5 μ L of aqueous uranyl acetate stain solution (1%) directly on a 200-mesh carbon-coated copper grid. After 30 s, the excess liquid was wicked away and the grids were air-dried.

Dynamic Light Scattering. DLS data were collected with a ManoPlus DLS nano particle size analyzer instrument (Particulate Systems, Norcross, GA). Three DLS measurements were obtained and averaged on aqueous solutions of CMP nanosheets at 20 °C. DLS melting experiments were conducted with a 1 cm path length cuvette at a heating rate of approximately 1 °C/3 min with a 50 s equilibration time at each degree.

Atomic Force Microscopy. AFM images were collected with an 628 Asylum MFP-3D atomic force microscope using tapping mode. 629 Images were obtained using ultrasharp AFM tips with a force constant 630 of 5 N/m and a resonance frequency of 150 kHz (Budget Sensors, 631 SHR-150). Images were collected at a scanning rate of 1 Hz. Samples 632 were prepared by drop-casting 20 μ L of peptide nanosheet solution 633 onto freshly cleaved mica. After 5 min, the solution was wicked away 634 and washed once with 30 μ L of HPLC-grade H₂O.

Small-Angle/Wide-Angle X-ray Scattering Measurements. 636 Synchrotron SAXS/WAXS measurements were performed at the 12-637 ID-B beamline of the Advanced Photon Source at Argonne National 638 Laboratory. The sample-to-detector distances were set such that the 639 overall scattering momentum transfer, q, range was achieved from 640 0.005 to 0.9 Å⁻¹, where $q = 4\pi \sin \theta/\lambda$, with 2θ denoting the 641 scattering angle and λ denoting the X-ray wavelength. The wavelength 642 was set at 0.9322 Å during the measurements. Scattered X-ray 643 intensities were measured using a Pilatus 2 M (DECTRIS Ltd.) 644 detector. Measurements were conducted on aqueous solutions of 645 CMP nanosheets at a concentration of \sim 2.5 mg/mL for $4R(X)_{444}$ @ 646 $4S(X)_{444}$ nanosheets and 4 mg/mL for $4R(X)_{444}$ and $4S(X)_{444}$ 647 nanosheets in 20 mM MOPS buffer (pH 7.0) at 5 °C. A quartz 648 capillary flow cell (1.5 mm diameter) was employed to prevent 649 radiation damage. The 2D scattering images were converted to 1D 650 scattering curves through azimuthal averaging after solid angle 651 correction and then normalizing with the intensity of the transmitted 652 X-ray beam using the software package at beamline 12-ID-B. The 1D 653 curves of the samples were averaged and subtracted with the 654 background measured from the corresponding buffers.

Cryogenic Transmission Electron Microscopy. The nanosheet sample was shipped and stored at 4 °C. Thereafter, it was briefly centrifuged to obtain a denser solution. Then 2 to 3 μ L of the suspension was pipetted onto a glow-discharged QuantiFoil grid 1.2/659 1.3 (300 mesh). Grids were blotted for 3 s with blot force 1 and foo plunge-frozen in liquid ethane using a Vitrobot with the environmental chamber set at 100% humidity and 4 °C. Data were acquired on a Titan Krios electron microscope at 300 keV (Thermo Fisher) in annoprobe mode, with a GIF Quantum LS Imaging filter (20 eV slit width) and a K2 Summit electron counting direct detection camera (Gatan).

Data sets at zero tilt were collected at a nominal magnifications of 105K and 130K, resulting in calibrated physical pixel sizes of 1.336 and 1.056 Å, respectively. The defocus was set in the range of 0.1–0.5 μ m. The data were collected with a modified in-house script using SerialEM. Every position was selected manually by the observation of crystal-like features, and each of these positions was exposed by recording a 14.4–16.8 s movie with 36–56 frames totaling 50 e⁻/Å².

The Focus software package⁴⁰ was used to drift correct the images 673 with Motioncor2. TCTF correction was done with Gctf. On the 674 basis of FFTs of collected frames, a selection was made between single 675 sheets and core—shell sheets. The unit cell of the 4R(X)₄₄₄@4S(X)₄₄₄ 676 nanosheets was confirmed for several images by measuring the 677 distances of the lattice in the local Fourier transformations and in the 678 real space. The images were filtered on the basis of a Wiener filter 679 approach, which enhances lattice features without knowledge or input 680 of the lattice parameters while assuming that the signal is uncorrelated 681 to the noise. These filtered images were analyzed and eventually 682 used as an overlay on the original drift-corrected images. Using 683 the filtered information as an overlay, it was possible to identify 684 locations of interest (i.e., lattice defects and distortions) over the 685 whole crystal.

Fluorescence Optical Microscopy. The Nikon Eclipse Ti 687 microscope was equipped with an Intensilight epifluorescence source 688 (Nikon), a CFI Apo 100 × NA 1.49 objective (Nikon), and a TIRF 689 launcher with three laser lines: 488 nm (10 mW), 561 nm (50 mW), 690 and 638 nm (20 mW). All of the reported experiments were 691 performed using the Quad Cube (cat. no. 97327) and TRITC 692 (96321) filter cube set supplied by Chroma.

Experiments were conducted using no. 1.5 glass slides (25 × 75 694 mm²) that were cleaned by sonication in Milli-Q (18.2 M Ω /cm) 695 water for 15 min, followed by a second sonication in 200 proof 696 ethanol for 15 min, and then dried under a stream of N2. The slides 697 were etched with piranha solution (v/v = 3:7 hydrogen peroxide/ 698 sulfuric acid) for 30 min to remove residual organic material and 699 activate hydroxyl groups on the surface. The cleaned substrates were 700 rinsed with Milli-Q water in a 200 mL beaker at least six times and 701 further washed with ethanol three. Slides were then transferred to a 702 200 mL beaker containing 2% 3-aminopropyl)triethoxysilane 703 (APTES) in ethanol for 1 h and then washed with ethanol three 704 times and thermally cured in an oven (~110 °C) for 10 min. The 705 APTES-functionalized slides were mounted to a custom-made 30-well 706 microfluidic chamber fabricated from Delrin. The nanosheet solutions 707 were added (10 μ L) to the wells and were immediately subjected to a 708 wash (3 × 100 μ L) with 20 mM MOPS buffer (pH 7.0). 709

ASSOCIATED CONTENT

S Supporting Information

The Supporting Information is available free of charge at 712 https://pubs.acs.org/doi/10.1021/jacs.9b09335.

MALDI-TOF MS, HPLC, TEM, AFM, CD, and cryo- 714 TEM data (PDF) 715

AUTHOR INFORMATION

The authors declare no competing financial interest.

ACKNOWLEDGMENTS

Notes

This work was supported by the NSF (CHE-1808509, V.P.C.) 726 and used resources of the Advanced Photon Source, a U.S. 727 Department of Energy (DOE) Office of Science User Facility 728 operated for the DOE Office of Science by Argonne National 729 Laboratory under contract no. DE-AC02-06CH11357. We 730 thank Prof. Tianquan Lian and Prof. Brian Dyer for the use of 731 the atomic force microscopy and DLS, respectively. We also 732 acknowledge the following people: Lubomir Kovacik and 733

734 Henning Stahlberg for their help with microscope operation 735 and the use of the cryo-TEM facility, respectively.

REFERENCES 736

- (1) Govindaraju, T.; Avinash, M. B. Two-dimensional nano-737 738 architectonics: organic and hybrid materials. Nanoscale 2012, 4 739 (20), 6102–6117.
- (2) Ariga, K.; Ji, Q.; Hill, J. P.; Bando, Y.; Aono, M. Forming 740 741 nanomaterials as layered functional structures toward materials 742 nanoarchitectonics. NPG Asia Mater. 2012, 4 (5), No. e17.
- (3) Ariga, K.; Ji, Q.; Nakanishi, W.; Hill, J. P.; Aono, M. 744 Nanoarchitectonics: a new materials horizon for nanotechnology. 745 Mater. Horiz. 2015, 2 (4), 406-413.
- (4) Boott, C. E.; Nazemi, A.; Manners, I. Synthetic Covalent and 746 747 Non-Covalent 2D Materials. Angew. Chem., Int. Ed. 2015, 54 (47), 748 13876-13894.
- (5) Zhuang, X.; Mai, Y.; Wu, D.; Zhang, F.; Feng, X. Two-749 750 Dimensional Soft Nanomaterials: A Fascinating World of Materials. 751 Adv. Mater. 2015, 27 (3), 403-427.
- (6) Colson, J. W.; Dichtel, W. R. Rationally synthesized two-753 dimensional polymers. Nat. Chem. 2013, 5, 453.
- (7) Zhang, H. Ultrathin Two-Dimensional Nanomaterials. ACS 754 755 Nano 2015, 9 (10), 9451-9469.
- (8) Ariga, K.; Watanabe, S.; Mori, T.; Takeya, J. Soft 2D 757 nanoarchitectonics. NPG Asia Mater. 2018, 10 (4), 90-106.
- (9) Zhang, S.; Zhang, J.; Fang, W.; Zhang, Y.; Wang, Q.; Jin, J. 758 759 Ultralarge Single-Layer Porous Protein Nanosheet for Precise 760 Nanosize Separation. Nano Lett. 2018, 18 (10), 6563-6569.
- (10) Zhang, X.; Xie, Y. Recent advances in free-standing two-761 762 dimensional crystals with atomic thickness: design, assembly and 763 transfer strategies. Chem. Soc. Rev. 2013, 42 (21), 8187-8199.
- (11) Sakamoto, J.; van Heijst, J.; Lukin, O.; Schlüter, A. D. Two-765 Dimensional Polymers: Just a Dream of Synthetic Chemists? Angew. 766 Chem., Int. Ed. 2009, 48 (6), 1030-1069.
- (12) Jin, H.; Guo, C.; Liu, X.; Liu, J.; Vasileff, A.; Jiao, Y.; Zheng, Y.; 767 Qiao, S.-Z. Emerging Two-Dimensional Nanomaterials for Electro-768 catalysis. Chem. Rev. 2018, 118 (13), 6337-6408.
- (13) Palma, C.-A.; Samorì, P. Blueprinting macromolecular 770 electronics. Nat. Chem. 2011, 3, 431. 771
- (14) Jia, X.; Minami, K.; Uto, K.; Chang, A. C.; Hill, J. P.; Ueki, T.; Nakanishi, J.; Ariga, K. Modulation of Mesenchymal Stem Cells 774 Mechanosensing at Fluid Interfaces by Tailored Self-Assembled 775 Protein Monolayers. Small 2019, 15 (5), 1804640.
- (15) He, X.; Hsiao, M.-S.; Boott, C. E.; Harniman, R. L.; Nazemi, A.; 777 Li, X.; Winnik, M. A.; Manners, I. Two-dimensional assemblies from 778 crystallizable homopolymers with charged termini. Nat. Mater. 2017, 779 16, 481.
- (16) Nazemi, A.; He, X.; MacFarlane, L. R.; Harniman, R. L.; Hsiao, 781 M.-S.; Winnik, M. A.; Faul, C. F. J.; Manners, I. Uniform "Patchy" 782 Platelets by Seeded Heteroepitaxial Growth of Crystallizable Polymer 783 Blends in Two Dimensions. J. Am. Chem. Soc. 2017, 139 (12), 4409-784 4417
- (17) Yu, B.; Jiang, X.; Yin, J. Size-Tunable Nanosheets by the 785 786 Crystallization-Driven 2D Self-Assembly of Hyperbranched Poly-(ether amine) (hPEA). Macromolecules 2014, 47 (14), 4761-4768.
- (18) He, X.; He, Y.; Hsiao, M.-S.; Harniman, R. L.; Pearce, S.; Winnik, M. A.; Manners, I. Complex and Hierarchical 2D Assemblies 790 via Crystallization-Driven Self-Assembly of Poly(1-lactide) Homopol-791 ymers with Charged Termini. J. Am. Chem. Soc. 2017, 139 (27), 792 9221-9228.
- (19) Evans, A. M.; Parent, L. R.; Flanders, N. C.; Bisbey, R. P.; 794 Vitaku, E.; Kirschner, M. S.; Schaller, R. D.; Chen, L. X.; Gianneschi, 795 N. C.; Dichtel, W. R. Seeded growth of single-crystal two-dimensional 796 covalent organic frameworks. Science **2018**, 361 (6397), 52-57.
- (20) Qiu, H.; Gao, Y.; Boott, C. E.; Gould, O. E. C.; Harniman, R. 798 L.; Miles, M. J.; Webb, S. E. D.; Winnik, M. A.; Manners, I. Uniform 799 patchy and hollow rectangular platelet micelles from crystallizable 800 polymer blends. Science **2016**, 352 (6286), 697.

- (21) Hudson, Z. M.; Boott, C. E.; Robinson, M. E.; Rupar, P. A.; 801 Winnik, M. A.; Manners, I. Tailored hierarchical micelle architectures 802 using living crystallization-driven self-assembly in two dimensions. 803 Nat. Chem. 2014, 6, 893.
- (22) Jiang, T.; Xu, C.; Liu, Y.; Liu, Z.; Wall, J. S.; Zuo, X.; Lian, T.; 805 Salaita, K.; Ni, C.; Pochan, D.; Conticello, V. P. Structurally Defined 806 Nanoscale Sheets from Self-Assembly of Collagen-Mimetic Peptides. 807 J. Am. Chem. Soc. 2014, 136 (11), 4300-4308.
- (23) Jiang, T.; Xu, C.; Zuo, X.; Conticello, V. P. Structurally 809 Homogeneous Nanosheets from Self-Assembly of a Collagen-Mimetic 810 Peptide. Angew. Chem., Int. Ed. 2014, 53 (32), 8367-8371.
- (24) Merg, A. D.; Touponse, G.; van Genderen, E.; Zuo, X.; 812 Bazrafshan, A.; Blum, T.; Hughes, S.; Salaita, K.; Abrahams, J. P.; 813 Conticello, V. P. 2D Crystal Engineering of Nanosheets Assembled 814 from Helical Peptide Building Blocks. Angew. Chem., Int. Ed. 2019, 58 815 (38), 13507 - 13512.
- (25) Egli, J.; Siebler, C.; Maryasin, B.; Erdmann, R. S.; Bergande, C.; 817 Ochsenfeld, C.; Wennemers, H. pH-Responsive Aminoproline- 818 Containing Collagen Triple Helices. Chem. - Eur. J. 2017, 23 (33), 819 7938-7944.
- (26) Park, S. H.; Yin, P.; Liu, Y.; Reif, J. H.; LaBean, T. H.; Yan, H. 821 Programmable DNA Self-Assemblies for Nanoscale Organization of 822 Ligands and Proteins. Nano Lett. 2005, 5 (4), 729-733.
- (27) Wittmann, J. C.; Lotz, B. Epitaxial crystallization of poly- 824 ethylene on organic substrates: A reappraisal of the mode of action of 825 selected nucleating agents. J. Polym. Sci., Polym. Phys. Ed. 1981, 19 826 (12), 1837-1851.
- (28) Williams, D. B.; Carter, C. B. Transmission Electron Microscopy: 828 A Textbook for Materials Science, 2nd ed.; Springer: New York, 2009; p 829 830
- (29) Palmstrom, C. J. Epitaxy of Dissimilar Materials. Annu. Rev. 831 Mater. Sci. 1995, 25 (1), 389-415. 832
- (30) Ohring, M. Materials Science of Thin Films: Deposition and 833 Structure, 2nd ed.; Academic Press: San Diego, 2002; Chapter 8, pp 834 417-494.
- (31) Gabrys, P. A.; Seo, S. E.; Wang, M. X.; Oh, E.; Macfarlane, R. J.; 836 Mirkin, C. A. Lattice Mismatch in Crystalline Nanoparticle Thin 837 Films. Nano Lett. 2018, 18 (1), 579-585.
- (32) Persikov, A. V.; Ramshaw, J. A. M.; Brodsky, B. Prediction of 839 Collagen Stability from Amino Acid Sequence. J. Biol. Chem. 2005, 840 280 (19), 19343-19349. 841
- (33) Okuyama, K. Revisiting the Molecular Structure of Collagen. 842 Connect. Tissue Res. 2008, 49 (5), 299-310.
- (34) Okuyama, K.; Xu, X.; Iguchi, M.; Noguchi, K. Revision of 844 collagen molecular structure. Biopolymers 2006, 84 (2), 181-191.
- (35) Jiang, T.; Vail, O. A.; Jiang, Z.; Zuo, X.; Conticello, V. P. 846 Rational Design of Multilayer Collagen Nanosheets with Composi- 847 tional and Structural Control. J. Am. Chem. Soc. 2015, 137 (24), 848
- (36) Qian, J.; Guerin, G.; Lu, Y.; Cambridge, G.; Manners, I.; 850 Winnik, M. A. Self-Seeding in One Dimension: An Approach To 851 Control the Length of Fiberlike Polyisoprene-Polyferrocenylsilane 852 Block Copolymer Micelles. Angew. Chem., Int. Ed. 2011, 50 (7), 853 1622-1625. 854
- (37) Gilroy, J. B.; Gädt, T.; Whittell, G. R.; Chabanne, L.; Mitchels, 855 J. M.; Richardson, R. M.; Winnik, M. A.; Manners, I. Monodisperse 856 cylindrical micelles by crystallization-driven living self-assembly. Nat. 857 Chem. 2010, 2, 566. 858
- (38) Moving towards the market. Nat. Mater. 2019, 18(6), 519-859 519.
- (39) Mastronarde, D. N. Automated electron microscope tomog- 861 raphy using robust prediction of specimen movements. J. Struct. Biol. 862 **2005**, 152 (1), 36-51.
- (40) Biyani, N.; Righetto, R. D.; McLeod, R.; Caujolle-Bert, D.; 864 Castano-Diez, D.; Goldie, K. N.; Stahlberg, H. Focus: The interface 865 between data collection and data processing in cryo-EM. J. Struct. Biol. 866 2017, 198 (2), 124-133.
- (41) Li, X.; Mooney, P.; Zheng, S.; Booth, C. R.; Braunfeld, M. B.; 868 Gubbens, S.; Agard, D. A.; Cheng, Y. Electron counting and beam- 869

- 870 induced motion correction enable near-atomic-resolution single-871 particle cryo-EM. *Nat. Methods* **2013**, *10*, 584.
- 872 (42) Zhang, K. Gctf: Real-time CTF determination and correction. *J.* 873 Struct. Biol. 2016, 193 (1), 1–12.
- 874 (43) van Genderen, E.; Li, Y.-W.; Nederlof, I.; Abrahams, J. P.
- 875 Lattice filter for processing image data of three-dimensional protein 876 nanocrystals. *Acta Crystallogr. D* **2016**, 72 (1), 34–39.
- 877 (44) Schindelin, J.; Arganda-Carreras, I.; Frise, E.; Kaynig, V.;
- 878 Longair, M.; Pietzsch, T.; Preibisch, S.; Rueden, C.; Saalfeld, S.;
- 879 Schmid, B.; Tinevez, J.-Y.; White, D. J.; Hartenstein, V.; Eliceiri, K.;
- 880 Tomancak, P.; Cardona, A. Fiji: an open-source platform for 881 biological-image analysis. *Nat. Methods* **2012**, *9*, 676.
- 882 (45) Schindelin, J.; Rueden, C. T.; Hiner, M. C.; Eliceiri, K. W. The
- 883 ImageJ ecosystem: An open platform for biomedical image analysis.
- 884 Mol. Reprod. Dev. 2015, 82 (7-8), 518-529.
- 885 (46) Schneider, C. A.; Rasband, W. S.; Eliceiri, K. W. NIH Image to
- 886 ImageJ: 25 years of image analysis. Nat. Methods 2012, 9, 671.